

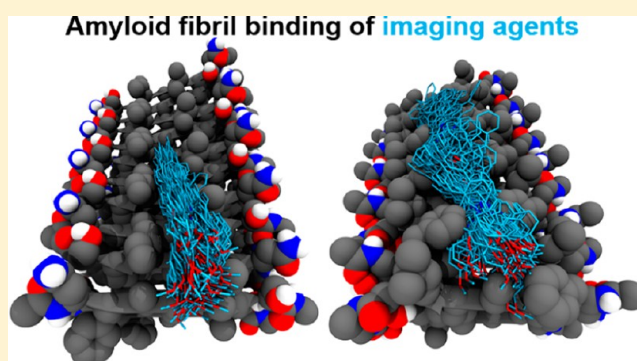
Identification of a Common Binding Mode for Imaging Agents to Amyloid Fibrils from Molecular Dynamics Simulations

Katrine Kirkeby Skeby, Jesper Sørensen,[†] and Birgit Schiøtt*

The Center for Insoluble Protein Structures (*inSPIN*), the Interdisciplinary Nanoscience Center (*iNANO*), and Department of Chemistry, Aarhus University, Langelandsgade 140, DK-8000 Aarhus C.

Supporting Information

ABSTRACT: Amyloid diseases are characterized by the misfolding and deposition of proteins in the body in the form of insoluble amyloid fibrils. Alzheimer's disease and type 2 diabetes mellitus are two examples of amyloid diseases which are closely related both with respect to the atomic structures of the amyloid fibrils and the disease pathology. Alzheimer's disease is very difficult to diagnose, and much research is being performed to develop noninvasive diagnostic methods, such as imaging with small-molecule agents. The interactions between amyloid fibrils and imaging agents are challenging to examine experimentally due to the insoluble nature of amyloid fibrils. This study uses molecular dynamics simulations to investigate the interactions between 13 aromatic amyloid imaging agents, entailing 4 different organic scaffolds, and a model of an amyloid fibril. Clustering analysis combined with free energy calculations are used to categorize and rank the resulting complexes. Several binding modes are identified across the different ligand scaffolds, however a common favorable binding mode can be identified in which the agent is placed in surface grooves along the amyloid fibril axis. The existence of multiple binding modes for imaging agents is proposed to originate from subtle differences in amino acid composition of the surface grooves on an amyloid fibril, resulting in fine tuning of the binding affinities for a specific amyloid fibril.



INTRODUCTION

Amyloid diseases are characterized by the misfolding of proteins into amyloid fibrils and subsequent deposition of amyloid aggregates in the body. More than 30 amyloid diseases have been described, among which are Alzheimer's and Parkinson's diseases and type 2 diabetes mellitus (T2DM).^{1,2} The defining property of an amyloid disease is the presence of amyloid fibril deposits composed primarily of the particular protein associated with the disease in question. In neurodegenerative amyloid diseases the deposits occur in the brain tissue, e.g., amyloid- β deposits in the brain of Alzheimer's disease patients.² In other amyloid diseases, deposits may occur systemically or localized in other tissues of the body, for instance in T2DM, fibrils composed of human islet amyloid polypeptide (hIAPP) deposit in the pancreas.²

The length and primary sequences of amyloidogenic peptides do not reveal a particular pattern, suggesting that amyloid fibril formation may be an intrinsic property of all peptides and proteins;² although, the 40-residue amyloid- β peptide ($A\beta_{1-40}$) and hIAPP share an overall of 25% sequence identity and 50% sequence similarity, with higher values in the central, fibril forming regions.³ The general structural motif of amyloid fibrils is termed the cross- β structure, which was first described in 1968 by Geddes et al.⁴ It can be identified by a characteristic pattern in X-ray fiber diffraction experiments.⁵ The cross- β

structure is composed of repeating units of β -strands arranged perpendicular to the fibril elongation axis (Figure 1a). This creates extended β -sheets with the hydrogen bonds aligned in the direction of the fibril.⁴ These β -sheets can be composed of parallel or antiparallel strands, and the sheets are usually paired, creating a double-layered β -sheet. The interface between the two sheets typically has complementary interlocking side chains, which excludes water molecules (Figure 1b). This is termed a steric zipper and can be composed of either inter- or intramolecular β -strands and be either in or out of register.⁶ The smallest structural unit of a fibril is termed a protofilament (Figure 1c).² It is usually composed of a number of β -sheets and has a width of around 2–5 nm.² Each fibril is composed of two to six twisting protofilaments, and the fully formed fibrils can be up to several micrometers in length.^{2,7} The structures of most amyloid fibrils, formed by full-length monomers, exhibit parallel β -sheets, however a recent structure of the $A\beta$ Iowa mutant contains antiparallel β -sheet topology.⁸

Atomic resolution structures of amyloid fibrils are difficult to attain due to their physical properties.⁹ Liquid-state NMR spectroscopy is not feasible due to the insoluble nature of the fibrils, and it has not been possible to prepare crystals suitable

Received: June 3, 2013

Published: July 16, 2013

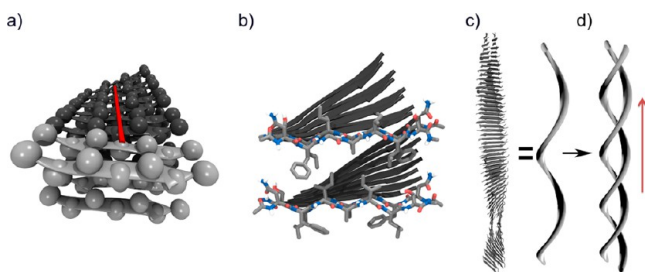
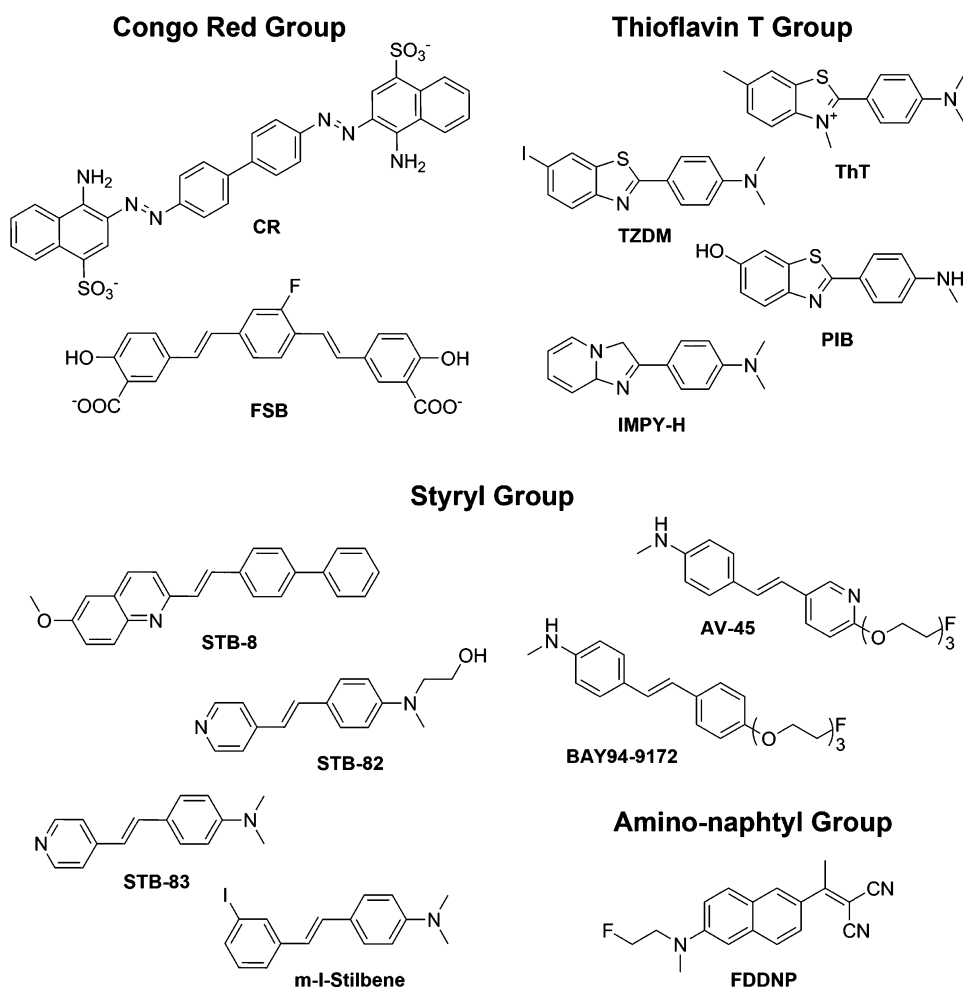


Figure 1. Structural levels of amyloid fibrils. (a) Schematic representation of a segment of an amyloid protofilament with the side chains represented by spheres. The red arrow indicates the fibril axis and is placed between the two central side chains of the peptide. The lighter coloring of the first two peptides in each β -sheet corresponds to the lighter colors in panel b. (b) Steric zipper interactions of interlocking side chains occur between two β -sheet layers. (c) Model of a protofilament which is composed of long twisted β -sheets which aggregate laterally to form the full fibril usually comprised of two to six protofilaments. (d) Model of mature fibril consisting of two protofilaments. The red arrow indicates the fibril direction equivalent to the direction of the red arrow in panel a.

for X-ray diffraction experiments of fibrils formed from the full-length peptides. However, in recent years, the atomic level structure of several amyloid fibrils has been published by use of solid-state NMR (ss-NMR) techniques,^{8,10–14} providing insight into the varieties of molecular topologies present among fibrils.¹⁵ For a review of ss-NMR studies of amyloid fibrils, see Tycko et al.¹⁶ In addition, X-ray crystallography has provided structural knowledge by using microcrystals of amyloid oligomeric assemblies of short peptides; though, these all lack the characteristic twist along the fibril axis.^{17–19} From molecular dynamics (MD) simulation, it was suggested that this lack of twist is caused by crystal packing effects.²⁰ A similar lack of twist was recently observed during the initial phases of the fibril formation process by AFM for the presumed fibrillating core of hIAPP,^{21,22} residues 20–29, when deposited on a mica surface.²³

The formation of amyloid fibrils is a nucleation-dependent mechanism analogous to the crystallization process.² The initial stage of the process is a lag phase in which the formation of the critical nucleus is the rate-limiting step. The lag phase can be eliminated by the addition of preformed fibrils, also termed

Scheme 1. Imaging Agents and Dye Molecules Included in This Study^a



^aCompound names: CR, Congo Red; FSB, (*E,E*)-1-fluoro-2,5-bis(3-hydroxycarbonyl-4-hydroxy)styrylbenzene; ThT, Thioflavin T; TZDM, 2-(4'-dimethylaminophenyl)-6-iodobenzothiazole; PIB, Pittsburgh compound B; IMPY-H, 2-(4'-dimethylaminophenyl)imidazo(1,2) pyridine; STB-8, (*E*)-2-(2-((1,1'-biphenyl)-4-yl)vinyl)-6-methoxyquinoline; STB-82, (*E*)-4-(4'-(*N*-methyl-*N*-hydroxyethyl)amino)styryl pyridine; STB-83, (*E*)-4-(4'-(*N,N*-dimethylamino)styryl) pyridine; m-I-Stilbene, (*E*)-4-*N,N*-dimethylamino-4'-iodostilbene; AV-45, florbetapir; BAY94-9172, florbetaben; FDDNP, 2-(1-{6-[(2-fluoroethyl(methyl)amino]-2-naphthyl)ethylidene]malono-nitrile).

seeds.² During the lag phase, β -sheet-rich assemblies termed protofibrils with diameters of 2–5 nm are generated.² These can be identified as beaded structures by AFM and TEM and should not be confused with the protofilaments.² Whether the protofibrils are on- or off-pathway intermediates is still debated.² The assembly of mature fibrils may occur by several different mechanisms including association of monomers to form structured aggregates, addition of monomers to preformed structured aggregates as well as association of larger oligomers to form the protofilament, which upon further aggregation gives the full fibril.²⁴ Phospholipid membranes have been reported to affect the fibril formation process, the observed effect depending on the lipid composition and conditions of the experiment.²⁴ Molecular simulations using both all-atom and coarse-grained representations of peptides and proteins have been shown to provide additional insight into the molecular level process.^{25–31}

The causative agent of amyloid diseases was for a long time thought to be the mature fibrils. This was based on the occurrence of large amounts of deposited amyloid in the organs of patients as well as the observation that amyloid- β fibrils were cytotoxic to neuronal cells.² Many aggregation intermediates (e.g., oligomers and protofibrils) and the fibril formation process itself have been implicated in the observed cytotoxicity.^{2,32} The precise mechanism of cytotoxicity has, however, not yet been elucidated, although indications are that membrane disruption may play a key role.^{33–35}

Noninvasive detection of fibrils in the brain of Alzheimer's disease patients using positron emission tomography (PET), magnetic resonance imaging (MRI), single-photon emission computed tomography (SPECT), or near-infrared fluorescence imaging is an area of research which is currently under much development.^{36–38} Some amyloid imaging agents have been tested in humans and have shown promise as new tools for use in monitoring the progression and diagnosis of Alzheimer's disease.^{37,39–41} Even though the amyloid fibrils are not believed to be the toxic species, amyloid can be identified in the brain tissue of patients with mild cognitive impairment which eventually leads to Alzheimer's disease.³⁷ The toxic species is presumably a precursor to amyloid fibrils, which suggests that the amount of fibril material could be used as a measure of cellular damage. Furthermore, it is not currently possible to make a definite diagnosis of Alzheimer's disease before an autopsy can be performed on the deceased patient. Therefore, a putative diagnosis is given based on observations of the decline of cognitive functions and exclusion of the possibility of other forms of dementia.⁴² Early diagnosis by amyloid detection, using imaging techniques, can aid in earlier evaluation of new disease modifying treatments as well as provide clues to the underlying disease pathology.^{37,43–46} This could be accomplished by monitoring the progression of amyloid deposition and thereby indirectly the events leading to the disease. The most successful approach to amyloid imaging has been the development of small molecules that bind specifically to amyloid fibrils. These have mostly been developed based on traditional amyloid fibril dyes, such as Congo Red (CR) and Thioflavin T (ThT) (Scheme 1).³⁶ Since the 1920s, CR has been used as a dye for the detection of amyloid fibrils in histological samples.⁴⁷ Binding to amyloid fibrils induces changes in the optical properties of CR, enabling the identification of amyloid fibrils.⁴⁷ CR has been reported by some to accelerate the fibril formation process and by others to inhibit the process.^{48–51} Either way, it can therefore not be used

as an *in situ* detection agent. ThT is another amyloid specific dye used to stain histological samples, exhibiting a change in fluorescence properties upon binding to amyloid fibrils.⁵² ThT is the most widely used *in situ* reporter to follow amyloid fibril formation,⁵² as it does not, or only to a minor extent, affect the fibril formation process.^{53–55} These dyes have been the lead compounds for the development of other amyloid staining compounds, although amyloid binding molecules not related to CR and ThT also exist.^{38,56} Most, if not all, of the dyes and imaging agents contain an aromatic group and have a rigid scaffold. So far, Pittsburgh compound B⁵⁷ (PIB) has been the most studied candidate for *in vivo* imaging,³⁷ however, 2-(1-{6-[(2-[fluorine-18]fluoroethyl)(methyl)amino]-2-naphthyl}-ethylidene)malononitrile (FDDNP) has also shown promising abilities to bind amyloid fibrils specifically and discriminate between the different stages of Alzheimer's disease.⁵⁸ The compound florbetapir (AV-45)⁵⁹ has just been approved by the American Food and Drug Administration for use in PET imaging of the A β fibril content of the brain and is sold under the name amyvid.⁶⁰ A novel class of styryl-based (STB) compounds has shown promise in mouse model studies as *in vivo* amyloid imaging agents using two-photon fluorescence imaging.⁶¹ The compound (E)-2-(2-((1,1'-biphenyl)-4-yl)-vinyl)-6-methoxyquinoline (STB-8) showed excellent blood-brain barrier permeability and specific staining of amyloid plaques.⁶¹ Several compounds are currently in clinical studies or have been tested in humans using PET technology.^{39,40,62–67}

The complexes between amyloid binding compounds and amyloid fibrils have been difficult to characterize structurally for the same reasons that amyloid fibrils are difficult to examine. The most studied compound is ThT, and the leading model for binding is termed the channel model.^{52,68} This places the ThT molecule along the fibril elongation axis in the regular grooves created by the repeating side chains of the amyloid fibril β -sheets, as indicated by the red arrow in Figure 1a.⁵² Based on NMR-experiments, Robbins et al. have recently suggested a model of ThT bound to amyloid fibrils formed from hIAPP in an upright position, i.e., parallel with the normal of the β -sheet plane.⁶⁹ The study suggested that several binding modes of ThT may be found and that several species may coexist on the fibril. One species was found to bind strongly to the fibril resulting in line broadening beyond detection in the liquid-state NMR spectrum.⁶⁹ This means that only the chemical shift changes in the more weakly bound species were available for structural determination. Therefore, the upright position of ThT proposed in the study corresponds to the weaker bound species.⁶⁹ The presence of multiple binding sites on A β has also previously been observed for the ThT class of compounds, although no structural information was reported.⁷⁰ Several MD simulations of ligand binding to models of amyloid fibrils have been published recently.^{71–77} These studies include both the binding of amyloid dyes,^{74,75} imaging agents,⁷⁶ and potential aggregation inhibitors^{71–73,77} and show that the imaging agents and dye molecules can bind in the regular grooves on the surface of the β -sheets,^{74–76} which correlates with the channel model of ThT.⁵² The aggregation inhibitors, however, show a slight preference for the fibril ends,^{71–73} thereby disrupting the possibility of further elongation. Amyloid imaging compounds can be grouped based on the molecular scaffold of the compound; CR, ThT, styryl-based, and amino-naphthyl-type ligands.³⁶ CR and ThT type ligands have been implied to have mutually exclusive binding sites on A β using radioligand competition assays, and thus they must bind noncompeti-

tively.⁷⁸ A distinct binding site for FDDNP has also been demonstrated by radioligand competition assays to Alzheimer's disease brain homogenates.⁷⁹

We have utilized an amyloid protofilament structure composed of peptide monomers with the sequence NFGAILS from hIAPP (residues 22–28) which was structurally solved by ss-NMR (PDB code 2KIB).⁸⁰ These residues are believed to form the central part of the fibrillating core of hIAPP.^{81,82} A structural model of the full-length hIAPP has been published recently based on combining ss-NMR and EPR data through simulations,¹³ however, it seems not to have been deposited to the RCSB protein databank. The cross- β structure therein contains hIAPP monomers regularly arranged in a hairpin fold with residues 20–29 occupying the turn region. Even though the β -sheets are parallel and residues 20–29, which are used in this study, are not actually part of the β -sheet region of the full fibril structural model, the surface features of the two fibrils are very similar, and the NFGAILS fibril shares properties with many other fibrils. The long surface grooves are present on both fibrils, and they both present all types of side-chains; hydrophobic, aromatic, and hydrophilic groups. Furthermore, the NFGAILS structure was determined by our collaborators which provides the possibility for future experimental testing of the results presented in this paper. These considerations merit the use of this fibril segment as a model system. The binding of small molecule dyes to the NFGAILS model, which includes the experimentally observed twist, was investigated using MD simulations. We obtained docking trajectories for ligand sampling of the fibril surface. We have chosen 13 different imaging agents and dye compounds. The reason for choosing these particular compounds was their prospective use as dyes or imaging agents for amyloids based on available experimental knowledge. The prospects of newer compounds as future *in vivo* amyloid imaging agents were considered important, as was chemical diversity among the compounds. It was recently recognized that there is a need for comparative studies of amyloid binding compounds.⁷⁷ Here, we investigate, to our knowledge, the largest number of amyloid ligands compared in a single MD study, providing a unique opportunity to study the general interactions between amyloid binding compounds and an amyloid fibril.

EXPERIMENTAL SECTION

System Setup. The binding of 13 different compounds (see Scheme 1) to an oligomeric segment of an amyloid protofilament of hIAPP composed of the assumed fibrillating core,^{21,22} hIAPP_{22–28}, consisting of NFGAILS peptide fragments, was investigated by MD simulations. This amyloid structure represents the basic building unit of the full hIAPP fibril and will therefore be referred to as a fibril in this study (Figure 1). Only the NFGAIL part of the hIAPP_{20–29} peptide was isotopically labeled, resulting in the structure of NFGAILS fragments being solved by ss-NMR (PDB code 2KIB).⁸⁰ The fibril in the current study contains double-layered β -sheets of the heptapeptide. To mimic the presence of additional residues, each peptide in the fibril was capped with an acetyl group at the N-termini and an amino methyl group at the C-termini. The fibril consists of two β -sheets, each containing 10 in-register antiparallel β -strands. Due to the antiparallel arrangement of the β -strands, the sides of the fibril (at the peptide terminals) have the same physical and chemical properties. The ends are also similar and are characterized by the protrusion of backbone amide groups. However, the two larger faces of the fibrils are different, and the properties are determined by the protruding side chains (Figure 1b). In the following, the face with Phe, Ala, and Leu will be termed the bottom surface, and the face with Asn, Gly, Ile, and Ser will be termed the top surface. The peptide was represented by the Duan

et al. all-atom point-charge force field (AMBER 03).⁸³ Three simulations using this amyloid structure were set up for each amyloid binding compound, consisting of one fibril segment and two identical ligands. By including two ligands in each simulation, the probability of binding is increased. To ensure that the starting position of the ligands with respect to the fibril did not bias the final binding position, it was varied between the three simulations (Figure 2). The ligands were placed at least 12 Å from the fibril structure.⁸⁰

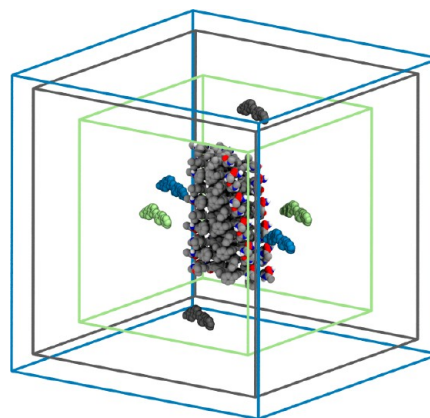


Figure 2. Setups for simulation A (gray), B (blue), and C (green). Due to the varying placement of the ligands in the initial setups, the simulation box size differs slightly between the setups.

Ligand Modeling. The ligands were built in Maestro 8.5 of the Schrödinger 2008 Suite software package.⁸⁴ Energy minimization was performed converging to a gradient of 0.05 kJ/(mol·Å) using a Polak–Ribière conjugate gradient algorithm in MacroModel 9.6.^{84,85} A conformational search to find minimum energy conformations of the compounds was performed using the low-mode conformational search algorithm^{86,87} for up to 10 000 steps in MacroModel 9.6.⁸⁴ Both minimizations and conformational searches were performed with the OPLS 2005 force field⁸⁸ as implemented in MacroModel 9.6⁸⁴ and using the GB/SA solvation model⁸⁹ to mimic water solvent. The electrostatic potential of the global minimum structure was obtained by geometry optimization at HF/6-31G* level using Gaussian 03,⁹⁰ as described in the protocol for developing new compatible parameters for the general amber force field (GAFF).⁹¹ Two of the molecules, m-I-Stilbene and TZDM contain iodine. The recommended basis set for generating GAFF parameters, 6-31G*, is not large enough to handle this, thus a bromine was used instead. Antechamber, as implemented in AMBER 9,⁹² was used to fit the atomic partial charges to the gas-phase electrostatic potential using the restrained electrostatic potential (RESP) method,⁹³ and the remaining ligand parameters were extracted from GAFF.⁹¹ All added ligand parameters can be found in the Supporting Information.

Simulation Protocol. All systems for MD simulations were built using the LEaP module of the AMBER 9 software package,⁹² and were solvated with TIP3P⁹⁴ water molecules in a cubic box with at least 10 Å from the nearest fibril or ligand atom to the box edge and then neutralized with either Na⁺ or Cl[−] ions. This resulted in systems with ~110 000/161 000/51 000 atoms, 36 000/53 000/16 000 water molecules and cubic box dimensions of 105/119/82 Å for setups A, B, and C, respectively (details in Table S1). The MD simulations were run in NAMD 2.6.⁹⁵ A time step of 2 fs was employed along with the SHAKE algorithm^{96,97} to constrain covalent bonds to hydrogen. Each system was minimized in four stages, each for 2000 steps. In stages 1–3, the positions of the protein, the backbone and the C α atoms, respectively, were constrained, and in the final stage no atoms were constrained. Following the protocol of Wu et al.,⁷¹ the system was heated from 0 to 500 K during 10 ps in the NVT ensemble, with the C α atoms constrained to their initial position. This was done to randomize the original positions and orientations of the ligands. Finally, two 10 ps equilibration simulations for all setups were performed at 300 K, and

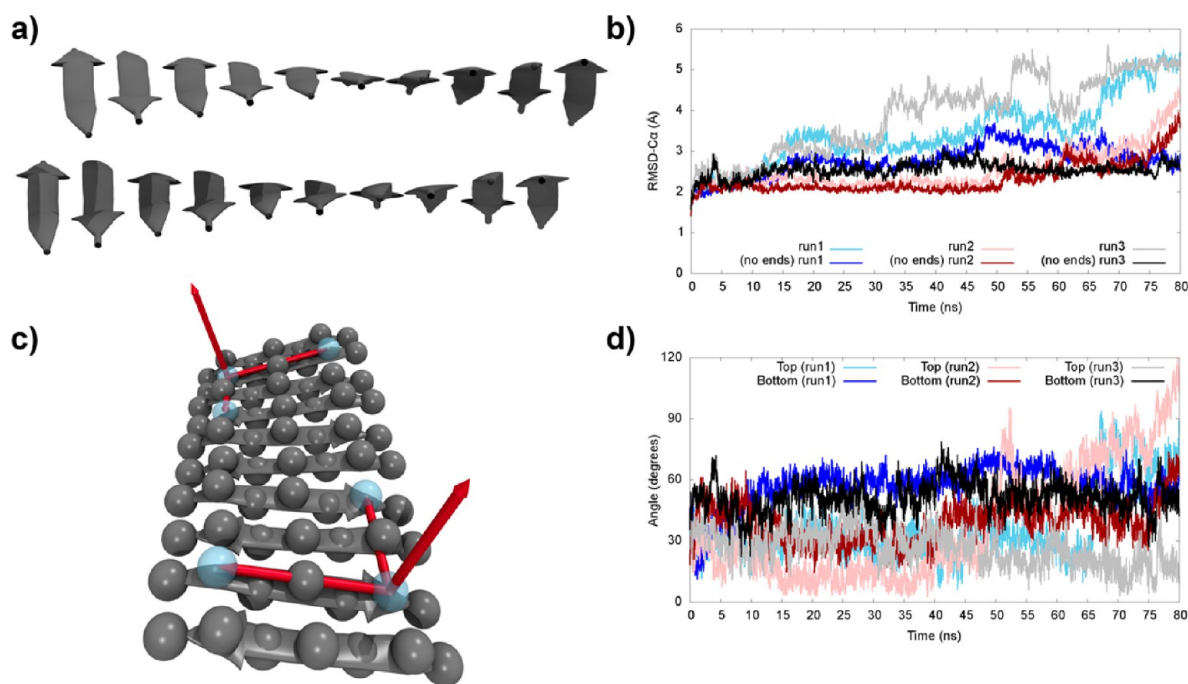


Figure 3. (a) The starting conformation of the fibril viewed from the side. (b) The C_{α} RMSD of the fibril simulations (run1, run2, and run3) without ligand present for all three runs. The RMSD is calculated for the entire fibril as well as for the fibril excluding the two protruding peptide strands (no ends) and is a running average over 20 ps. (c) The twist angle of the β -sheets is measured as the angle between the β -sheet normals at each end of the fibril. (d) The twist angle of the two β -sheets of the fibril is a running average over 20 ps.

in the first stage the C_{α} atoms were restrained, whereas in the last stage everything was free. For each system, 20 ns of production dynamics was performed. Triplication runs of each ligand were performed using two ligands in each simulation box with the starting positions chosen as shown in Figure 2, giving 3×20 ns = 60 ns of simulation for each of the 13 ligands. Splitting the simulations into two trajectories, one for each ligand, results in a total of 120 ns of trajectories for analysis per ligand. Since, a snapshot was saved every 2 fs, a total of 60 000 snapshots were available for analysis per ligand. The equilibration and production simulations were performed in the isothermal–isobaric (NPT) ensemble at 300 K and 1.01325 bar. The temperature was held constant using Langevin dynamics with a damping coefficient of 2 fs^{-1} not including hydrogen atoms. The pressure was maintained using a Nosé–Hoover Langevin piston,^{98–100} with a piston period of 200 fs, a piston decay time of 100 fs, and a piston temperature of 300 K. Periodic boundary conditions were used to eliminate boundary effects, and the particle mesh Ewald method with a grid spacing of 1 Å was employed to calculate the electrostatic interactions of the system.^{101–103} The van der Waals interactions were cut off at 10 Å, with a switching potential added at a distance of 9 Å. The pair list included pairs of atoms within 11 Å and was updated every 20 steps. To test the parameters of the ligands, they were each simulated for 20 ns in a water box. For comparison, three simulations of the fibril without ligands present were also performed for 80 ns each. These simulations were only heated to 300 K.

Analysis of Trajectories. For analysis the three simulations for each ligand were divided into two trajectories, each containing one of the two ligands. The resulting complexes from the trajectories were analyzed based on the position and orientation of the ligand relative to the fibril. The collected snapshots were aligned on the C_{α} atoms of the fibril and clustered based on the position of the heavy atoms of the ligands. Only molecular complexes containing >20 atomic contacts below 5 Å between any fibril atom and any ligand atom were included in the clustering analysis. Several clustering algorithms were initially tested, and the following variation of an agglomerative clustering scheme¹⁰⁴ that gave well-defined and spherical clusters was used: (i) combine the two structures with the lowest internal RMSD to initiate a cluster; (ii) find the snapshot with the lowest RMSD relative to the

average structure of the current cluster and add it to the cluster; (iii) a cluster is complete when the snapshot with the lowest RMSD with respect to the average structure of the current cluster is larger than 5 Å; and (iv) restart from (i) to form a new cluster unless the RMSD between all remaining pairs of snapshots is larger than 5 Å. The representative structure of a cluster is the snapshot with the lowest RMSD to the average position of atoms in the cluster. Only clusters with >1% of the total number of saved snapshots (equal to at least 600 structures in a cluster) for one ligand were considered for further analysis ensuring statistical significance.

Free Energy Calculations. For calculation of the binding free energy between the imaging agent (L) and the fibril (R), the molecular mechanics Poisson–Boltzmann surface area (MM-PBSA) method is applied as implemented in AMBER 11.¹⁰⁵ Therein the difference in binding free energy of a given ligand is computed as the difference in free energy between the product (LR) and the reactants (L + R):

$$\Delta G_{\text{binding}} = G_{\text{LR}} - (G_{\text{R}} + G_{\text{L}}) \quad (1)$$

The MM-PBSA approach estimates the energy of each species as follows:¹⁰⁶

$$G = \langle E_{\text{MM}} \rangle + \langle G_{\text{solv}} \rangle + T \langle S \rangle \quad (2)$$

In eq 2, E_{MM} is the enthalpic contribution to the free energy, G_{solv} is the solvation free energy, T is the temperature, S is the entropy of the species, and $\langle \rangle$ denotes an ensemble average. E_{MM} is extracted directly from the force field and is therefore a sum of the bonded and nonbonded contributions. G_{solv} is calculated using an implicit solvent approach as a sum of a polar (E_{PB}) and a nonpolar term (E_{cav}). The polar term, E_{PB} , is calculated using the Poisson–Boltzmann equation, and E_{cav} represents the energy required to make a ligand-sized cavity in the implicit solvent and is found to be proportional to the solvent accessible surface area of the molecules.¹⁰⁷ The entropy can be estimated either from normal-mode analysis or by quasiharmonic analysis.¹⁰⁶ These methods are computationally expensive and require extensive sampling to reach convergence. As the goal here is to calculate relative binding free energies between similar ligands, the assumption that the change in entropy upon binding is similar for all ligands has been applied, which is a commonly used approximation

and has been shown previously to lead to effective ranking of ligands.¹⁰⁸ The trajectories for both ligands and fibril are extracted from the same simulation using the single-trajectory approach.¹⁰⁹ This approach effectively minimizes the noise from sampling inconsistencies and the error inherent in the force field and in the implicit solvent method.¹¹⁰ The binding free energy of each cluster was calculated using the MMPBSA.py script as implemented in AMBER 11.¹¹¹ No cutoff was used for the nonbonded interactions, and the dielectric constant was set to 1 for the solutes and 80 for the solvent. The ionic strength was set to 0 M in all the calculations for consistency and to match conditions of the simulations. The solvent probe radius was 1.4 Å mimicking a water molecule.

Degree of Burial. The degree of burial is calculated as the fraction of the surface area of the ligand that is excluded from water upon contacting the fibril. The total surface area of the ligand and the buried surface area are calculated from the same trajectory snapshot. The degree of burial for the clusters is an average over all snapshots in a cluster.

RESULTS

To investigate the stability of the fibril structure, MD simulations of the fibril without ligands present were performed for 80 ns in triplicate runs (run1, run2, and run3). The starting fibril structure is shown in Figure 3a. In run1 and run3, the C_α RMSD (Figure 3b) is continuously rising, reaching 5 Å after 80 ns. This is caused by a shearing motion between the two β -sheets, resulting in one peptide strand protruding at each end of the fibril, as has also previously been observed for fibrils of the hIAPP_{22–29} peptide.¹¹² Therefore, the RMSD is also reported for the fibril excluding the two end strands that are exposed. The RMSD of the central part of the fibril is seen to be reasonably constant below 3 Å, indicating that the observed increase in RMSD for run1 and run3 originates from these two end-strands. The increase in the RMSD caused by the end strands is speculated to be caused by a lack of the steric zipper interactions for these, which make them prone to break off the fibril in the simulation, as all that holds them in place are nonbonded interactions and hydrogen bonds to the backbone atoms of the adjoining peptide in the same β -sheet. The RMSD of the fibril in run2 is approximately constant for the first 45 ns, after which it also increases steadily, and is still rising at 80 ns. The origin of this increase in RMSD is an additional twist of the top β -sheet layer of the fibril (Figure 3d). The twist angle of the fibril is defined as the angle between two normals of a β -sheet. The normal is defined at each end of the fibril measured at the second peptide strand to avoid the abnormalities from the loose end peptides (Figure 3c). The angle has been calculated for the two β -sheets individually. As the deformations of the fibril all seem related to the relatively small size of the fibril and do not appear until after 30–50 ns, the 20 ns simulations of the amyloid fibril, including ligands, are expected to contain a stable fibril structure without artificial unfolding and twisting, which was further examined by calculations of C_α RMSD curves and the twist angle of the fibril model.

In the following, STB-8 will be used as an example throughout the analysis of ligand binding to highlight the trends observed for all the ligands. Similar data for the remaining ligands can be found in the Supporting Information. When referring to a particular simulation and ligand, the following nomenclature will be used: compound-setup_{ligand}; e.g., STB-8-B_{lig1} refers to a simulation with STB-8 and the trajectory of ligand 1 as sampled in setup B (Figure 2).

The C_α RMSD remains constant around 2 Å for STB-8-A and -C (Figure 4a), indicating stable fibrils at the 20 ns time

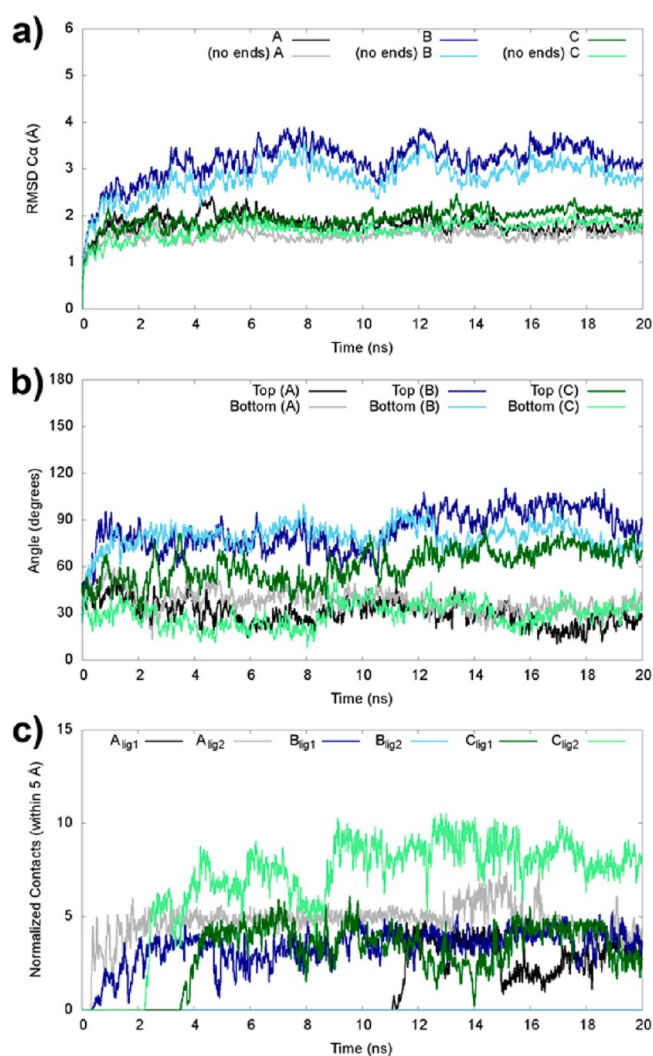


Figure 4. (a) C_α RMSD of the fibril as a function of time in the three simulations (A–C) with STB-8. The curves are running averages over 20 ps. (b) The twist of the β -sheets is a running average over 20 ps. (c) Atomic contacts of STB-8 with the fibril within 5 Å are plotted for all STB-8 molecules. These are also running averages over 20 ps. Plots for the rest of the ligands can be found in the Supporting Information.

scale. This is representative for all the ligand binding simulations (figures for the remaining 12 ligands are found in Figure S1). The C_α RMSD curves of the fibril fluctuates around 2.5 Å for most of the simulations, which is comparable to the simulation of the fibril alone and is reasonable for this size of peptide assembly. The higher RMSD observed for STB-8-B is due to an additional twist of the fibril (Figure 4b). Some of the RMSD curves do not level off, which could be a consequence of the ligands binding to the fibril. Yet, since the simulations of the fibril alone also did not level off, it is more likely a result of the fibril being flexible. The flexibility of the fibrils arises from protruding peptide termini or additional twisting of the fibril. It is generally not affected by the binding of ligands, which is realized by comparing the contact plots with the RMSD curves (Figures S1 and S3). This can be exemplified by ThT-B, which has one of the highest RMSD values, however, the fibril does not bind a ligand until after 15 ns. It seems that the binding of ligands may slightly reduce the flexibility of the fibrils, since it is only in two (STB-83-A and ThT-B) out of 39 simulations where the RMSD of the fibril significantly exceeds 3 Å after 20

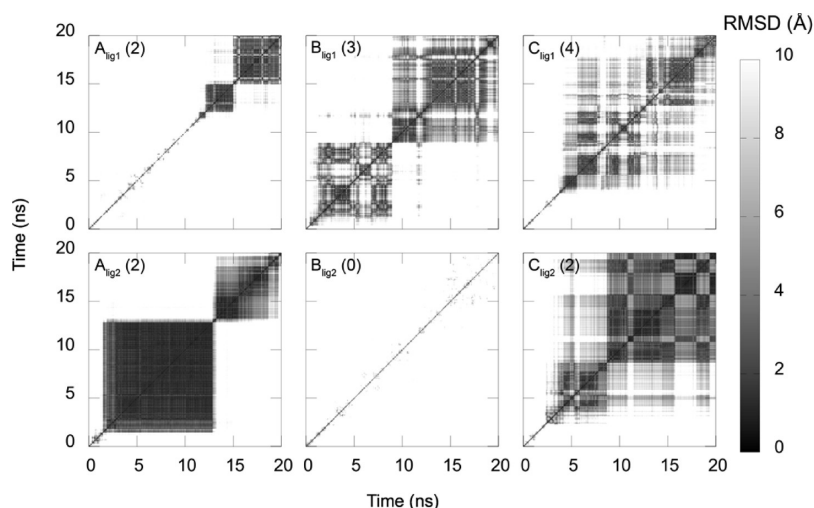


Figure 5. RMSD matrices for STB-8. The fibril is aligned by the C_{α} atoms to the starting structure, after which the ligand heavy-atom RMSD is calculated between all pairs of snapshots. A dark square indicates that the ligand stays in approximately the same binding mode. The numbers in parentheses are the number of clusters identified by the clustering analysis. RMSD matrices for the remaining ligands can be found in the Supporting Information.

ns, which is approximately the maximum value for the fibril simulations (run1, run2, and run3) at 20 ns. For both STB-83-A and ThT-B, an additional twist of the fibril is found to cause the increase in RMSD (compare Figures S1 and S2).

The dynamics of ligand binding to the fibril can be illustrated by the number of atomic contacts between the ligand and the fibril normalized by the number of heavy atoms in the ligand (Figures 4c and S3). A difference in the number of molecules that bind to the fibril for each ligand is observed. This depends on the random diffusion of the ligand as well as the binding affinity of the ligand for the fibril. Several examples of binding and unbinding of the ligands are encountered, e.g. STB-8- C_{lig1} at 14 ns (dark green in Figure 4c). This indicates that binding is a dynamic process and that the fibril–ligand complex is not a sticky encounter resulting from trapping the ligands and fibril out of water phase. Instead, the resulting complexes are specific low-energy structures. This is also reflected by the slow rise in contacts for a few of the molecules, which is due to the ligand searching the surface of the fibril for a preferred binding position, e.g., STB-8- C_{lig2} (light green in Figure 4c). At least one molecule out of the six for each of the 13 ligands shows atomic contacts within 5 Å of the fibril during the simulations (Figure S3). The number of contacts that a given ligand makes to the fibril depends on the particular binding position, and it can be observed that the charged ligands (CR, FSB, and ThT) do not make as many contacts per heavy atom as the more hydrophobic ligands, e.g., STB-82. (Figure S3) It is also seen that the number of contacts varies even for a single ligand, which suggests varying levels of burial on the fibril (Figure 4c).

In four of the simulations (AV-45-C, FDDNP-A, FDDNP-B, and IMPY-H-A), the two ligands in the simulation box formed a dimer before binding to the fibril. The ligands were at least 20 Å apart, and each ligand is at least 12 Å from the fibril, initially in the simulations. This should make the ligands more prone to encounter the fibril before they encounter each other. However, the ligands diffuse quite rapidly, which in this case leads to the ligand dimerization across the periodic boundary prior to fibril binding. Dimerization of ThT has been suggested in the context of amyloid fibril binding and fluorescence as an excited dimer,^{113,114} however, this is not observed in this study.

The recognition and binding process, ultimately resulting in a stable binding position of the ligand on the fibril surface, is different for each ligand. From an RMSD matrix of the ligand heavy atoms after alignment of the fibril it can be visualized how the stability of the fibril–ligand complexes varies (Figures 5 and S4). Some ligands find a stable binding mode very quickly, e.g., STB-8- A_{lig2} , while others probe the surface of the fibril, finding several less stable binding modes, e.g., STB-8- C_{lig1} . Even if a stable binding mode has been found, the ligand can still move on the surface of the fibril, which is seen for STB-8- A_{lig2} after ~13 ns.

The structural details of the different binding modes of the ligands are not visually evident from an RMSD matrix, therefore clustering analysis of the ligand trajectories was performed. The number of clusters obtained from a simulation correlates very well with the appearance of the RMSD matrices (Figure 5). The resulting clusters were structurally analyzed and merged into binding modes based on the position and orientation of the ligand on the fibril (Figure 6). This was performed by visual inspection of the clusters. The position of the ligand refers to the face of the fibril, where the ligand is bound; top, bottom, sides, or ends. As discussed in the Experimental section, the different surfaces of the fibril display different chemical environments. The fibril consists of two layers of in-register, antiparallel β -sheets. The two sides of the fibril are identical and are characterized by the presence of acetyl and N-methyl capping groups. The ends, which are also identical, display free backbone amide and carbonyl groups as well as exposed side chains. The top and bottom faces, however, are different, each containing a pattern of repeating side chains which create grooves along the length of the fibril. The top face contains three grooves (Figure 6a); the central groove on the top face is created by isoleucine residues, while the minor side grooves are created by isoleucines on one side with alternating serines and asparagines on the other side. The bottom face effectively only contains one groove, since the side chains of the phenylalanines are leaning toward the alanine residues which excludes the ligands from binding in the two minor grooves (Figure 6a). However, the small side chain of alanine allows room for a small hydrophobic central groove on

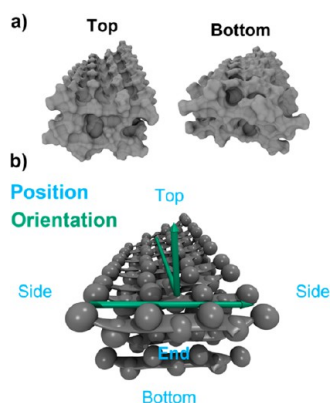


Figure 6. Characterization of binding modes based on position and orientation of the ligand. (a) Surface representation of the top and bottom surfaces of the fibril. The top face contains a large central groove between the leucine side chains and two minor side grooves. The bottom face has no extended linear groove as found on the top, rather a shallow crevice is seen. (b) Position of the ligand refers to the end, side, top, or bottom face of the fibril. The ligand orientation is described by the long axis of the ligand being parallel with the fibril axis, the peptide strands, or the β -sheet normal, as indicated by the green arrows.

the bottom face. These types of grooves along the fibril are expected to be present on all amyloid fibrils due to the generic cross- β structure, although the binding specificity is likely determined by subtle differences in the specific side chains present on the surfaces. The orientation of the ligand refers to whether it is parallel to the fibril axis, the peptide strands, or the β -sheet normal (Figure 6b). Binding modes are referred to with the following convention: position_{orientation}.

Binding occurred to all four faces of the fibril, however not all orientations were observed for all faces. Binding to the top and bottom face, parallel with the fibril, is furthermore subdivided

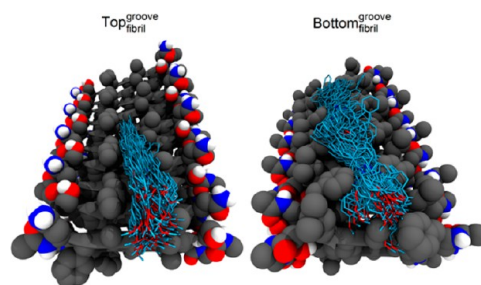


Figure 8. Example of the top_{groove_fibril} and bottom_{groove_fibril} binding modes for STB-8. The fibril is shown in gray, and snapshots of the ligand are shown in light blue. Oxygen, nitrogen, and hydrogen are shown in red, blue, and white, respectively, on both the fibril and ligand.

into two binding modes; either the ligand inserts into a groove or binds on top of the side chains. This analysis resulted in 12 different binding modes with calculated populations as shown in Figure 7.

The two binding modes with highest populations are top_{groove_fibril} and bottom_{groove_fibril}, both with around 20% of all complexes (Figure 7). In these two binding modes the ligand is embedded in the hydrophobic surface grooves parallel to the fibril elongation axis (Figure 8). It is interesting to note that no ligands bind in the side grooves on the top face, which may be due to the more polar nature of these grooves. In total, the bottom face has the highest population (37.6%). This is speculated to be caused by the possible π - π interaction between the phenyl rings of the side chains and the highly aromatic ligands. Bottom_{side chains_fibril} and bottom_{peptide} are also quite populated, since it is not necessary to position the ligand inside the groove to be able to contact the phenyl groups. Top_{normal}, top_{peptide}, and top_{side chains_fibril} all have negligible populations. This indicates that initial contact on the top face quickly leads to insertion of the ligand into the central groove.



Figure 7. Calculated population of the identified binding modes and the estimated free energy of binding of the individual clusters. The population of a binding mode (including all clusters belonging to each binding mode) is represented by the fraction of snapshots in the binding mode of the total number of clustered snapshots which is 271 481. Each point in the graph represents the MM-PBSA binding free energy of a single ligand cluster. Lower energy means a higher binding affinity. Table S2 contains the data used for creating this figure including standard deviations of the binding energies.

The side faces are also quite populated, with an even distribution between orientations either parallel with the fibril axis or the fibril normal. This reflects that the side face has no features that govern a specific orientation of the ligand, which could be a consequence of the less polar nature of the side faces, due to the peptide-mimicking capping groups on the peptides. Binding on the side faces is, however, difficult to interpret since the capping groups are not present in the decamer fibril for which the structure was determined.⁸⁰

Binding at the ends of the fibril is not highly populated, which indicates that this is not a relevant binding mode for the chosen imaging agents. This was an encouraging observation since the concentration of fibril ends *in vivo* will be low due to the, normally, very long amyloid fibrils, and had the end binding been preferred, a less sensitive agent would be expected. The clusters at the end faces contain ligands belonging to the styryl-based and ThT families of compounds. Two of the ligands (STB-82 and IMPY-H) result in clusters belonging to the $\text{end}_{\text{fibril}}$ binding mode, where the ligands are sandwiched between the two β -sheets in the central groove, with the ligand axis parallel to the fibril elongation axis. This creates a binding mode, which is similar to $\text{top}_{\text{fibril}}^{\text{groove}}$ and $\text{bottom}_{\text{fibril}}^{\text{groove}}$, though with the ligand interacting with both top and bottom β -sheet layers. Some of the ligands in $\text{end}_{\text{peptide}}$ are also positioned between the two sheets. Inhibition of or influence on fibril formation by STB-82 and IMPY-H has, to our knowledge, not been reported. However, it has been reported for CR and several other small molecules.^{48,49,51,115} Binding between the two β -sheets at the ends of the growing fibrils may present a likely mechanism for the inhibition process.

Some bias of the binding position of the ligand from its initial position in the simulation box may be present in the simulations, since 17 of a total of 42 bound ligands contact the same face as they were placed at a distance from. If the face that a ligand binds to is completely random, one-sixth of the total number of ligands should bind to the same face, so seven ligands out of 42. However, the surface area and the affinity of the ligands for the faces should also be factored in. Three of the 17 bind to the end face, four each to the side and bottom faces, and six to the top face. Since this is quite evenly distributed among the four types of faces and the ligands were positioned with regard to all six faces in the setup of the simulations, it is not likely that the starting position has biased the results significantly.

There seems to be a trend toward the ligands preferring the top and bottom faces of the fibril (Figure 9). Eight out of 13 ligands populate the bottom face highest. Two have the side as most populated, and three have the top as the most populated face. This means that combined, 11 out of 13 ligands prefer to bind the faces of the fibril containing the surface grooves. The ThT group of ligands has the most snapshots on the bottom face for all ligands except TZDM, which only leads to a single cluster. This indicates that the ThT group prefers the bottom face. In the styryl-based group of ligands, AV-45 and BAY94–9172 do not bind to the bottom face. However, examining only the snapshot count might not be the best measure, since bias of the binding position and the relative sizes of the faces could have an influence on the result. Therefore, it is important to also consider the energetics of the binding.

The calculated MM-PBSA binding free energies are reported in Figure 7. It is clear that the clusters in $\text{top}_{\text{fibril}}^{\text{groove}}$ and $\text{bottom}_{\text{fibril}}^{\text{groove}}$ have the most favorable binding energies since

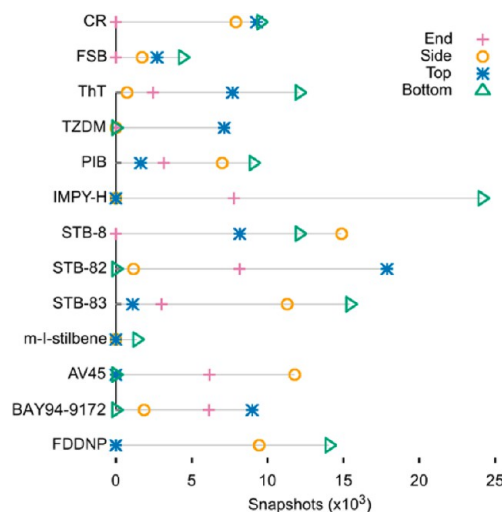


Figure 9. Number of clustered snapshots for each ligand on the four faces of the fibril.

they have the highest number of clusters with low energies (> -15 kcal/mol) and no less favorable clusters (energies > -10 kcal/mol). This is consistent with the previous observation that these two modes are the most populated. A few clusters on the end face also display favorable binding free energies, which may be due to the large number of favorable contacts that results when the ligand binds between the two β -sheets. This is seen by the large number of contacts per ligand heavy atom observed in the trajectories from which these two clusters arise (Figure S3, STB-82- A_{lig2} and IMPY-H- C_{lig2}). Most of the clusters on the side faces have quite low binding affinities, except for three CR clusters. This may indicate that binding to the sides is a consequence of the large surface area. Even though the bottom face has the highest number of snapshots for more ligands than the top face, it seems that $\text{top}_{\text{fibril}}^{\text{groove}}$ has a slightly higher binding affinity than $\text{bottom}_{\text{fibril}}^{\text{groove}}$. Furthermore, the two clusters in $\text{bottom}_{\text{fibril}}^{\text{groove}}$ with highest binding affinities are the CR clusters, which are found to be special, as will be discussed below.

The degree of insertion of the ligands into surface grooves of the fibril can be quantified by the burial percentage of the ligands belonging to the individual clusters. The burial percentage for all the clusters as a function of the binding energy is depicted in Figure 10. A trend is clear; the larger degree of burial, the more favorable the binding is, though some variations are seen. It is evident that the majority (11 out of 14) of the clusters with burial percentages of $>60\%$ are from the $\text{top}_{\text{fibril}}^{\text{groove}}$ and $\text{bottom}_{\text{fibril}}^{\text{groove}}$ binding modes. The high degree of burial of these binding modes is likely due to the complementarity of the surface grooves with the linear shape of the ligands. The clusters which have both low binding energy (< -20 kcal/mol) and high burial percentages ($>60\%$) are all except one (which belongs to $\text{end}_{\text{fibril}}$) from the $\text{top}_{\text{fibril}}^{\text{groove}}$ binding mode. The lack of clusters from the $\text{bottom}_{\text{fibril}}^{\text{groove}}$ binding mode is likely due to the shallow groove on this face of the fibril, since internal strain or steric clashes in the peptides or ligand that lowers the binding energy could occur, when the contact surface between the ligand and the fibril is increased. The cluster from the $\text{end}_{\text{fibril}}$ binding mode with $\sim 70\%$ burial is the IMPY-H cluster where the ligand binds between the two β -sheets.

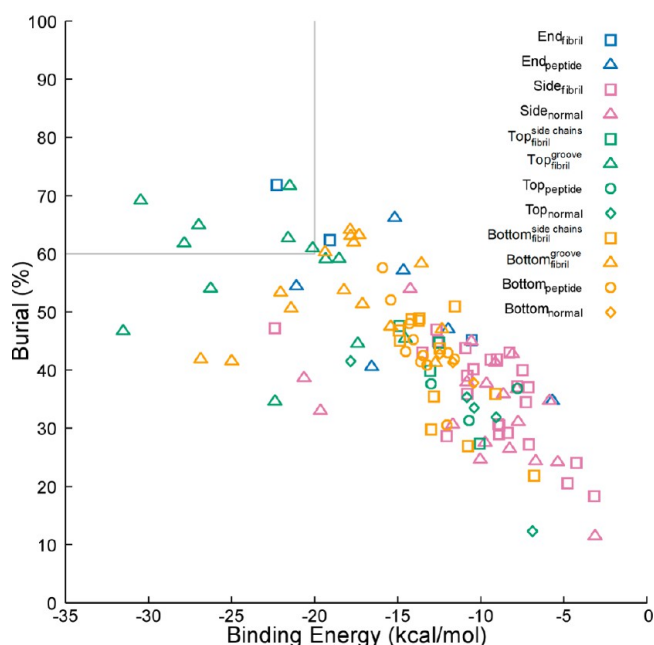


Figure 10. Calculated degrees of burial for all clusters as a function of the binding energy of the cluster. The burial percentage is calculated as the average ligand surface area that is lost upon association with the fibril, therefore, burial of 100% means that the ligand does not have any solvent accessible surface. The exact numbers and standard deviations are available in Table S2.

The more polar and charged ligands have lower degrees of burial (Figure S5 and Table S2). CR, FSB and ThT, which are charged, and AV-45 and BAY94-9172, which have polyethylene-glycol chains, have at most one cluster which is >50% buried. This behavior is to be expected since it is unfavorable to bury the polar parts of the ligands.

The preference of the ligands for binding in the top and bottom central grooves becomes obvious when displaying representative structures of the clusters in colors according to the calculated free energy of binding of the cluster (Figures 11 and S6). It is evident that the clusters buried in the hydrophobic grooves have a more favorable binding free energy than clusters that are on the surface of the fibril.

The contributions to the total binding free energy as outlined in eq 2 are reported in Figure 12a and have been calculated for a given cluster as the fraction of the energetic components of the total energy and using a population-weighted averaging over all clusters for a given ligand. A positive number thus represents a favorable contribution to the binding energy, and a negative number is an unfavorable contribution to the binding energy. The polar solvation contribution to the binding energy (ΔE_{PB}) is unfavorable for all ligands. The most favorable contribution to the energy is, not surprisingly, the nonpolar interactions. CR and FSB have higher contributions from electrostatic interactions than the remaining ligands, due to their negative charges. Among the neutral ligands, the more polar ones, such as AV-45 and PIB, have more unfavorable contributions from the polar solvation energy (E_{PB}). The lower electrostatic interaction energies of the polar neutral ligands demonstrate that the polar parts of the ligand is not interacting with the fibril, which correlates well with the lower burial percentage of e.g. AV-45 (Figure S5). This reflects that the electrostatic interactions with the solvent compared to the fibril are more favorable for these two ligands compared to the other

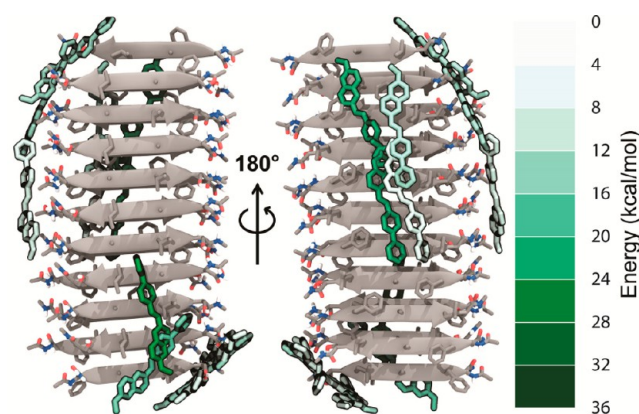


Figure 11. Representative structures of the STB-8 clusters, colored by the free energies calculated for the cluster. The left figure is a view of the top layer, and the right is a view of the bottom layer. The representative is the structure with the lowest RMSD to the average structure in the cluster. For clarity, the fibril structure shown is the minimized starting structure. Representative structures for clusters of the 12 other ligands can be found in Figure S6.

neutral ligands. However, all ligands have electrostatic interactions which are more favorable with the solvent than the fibril. Therefore, to move the polar molecules from the polar water to the nonpolar surface of the fibril requires more energy than for the nonpolar molecules.

Combining the absolute energetic contributions into a polar and a nonpolar part for all the ligands allows us to compare the ligands on an absolute scale (Figure 12b). The polar contribution to the binding energy falls within a narrow range for most of the clusters for a given ligand. It is the nonpolar contribution of the interaction between the ligands and the fibril that drives the binding, which is not unexpected from their chemical structures; they are all mostly nonpolar. Furthermore, due to the narrow range of polar interaction energies, it seems that the variation in the nonpolar contribution determines the binding affinity. This is in agreement with the observation that binding in the hydrophobic grooves on the fibril should be the most favorable, since this allows for maximizing the hydrophobic interactions. One ligand that seems to have slightly higher and more variation in the polar energy is CR. However, its nonpolar energy is also much more favorable than observed for the other ligands, which compensates for the more unfavorable polar interaction.

CR stands out as having a very favorable binding free energy in almost all of the clusters. This may be due to the large size of CR, which provides the possibility for a high number of favorable contacts. This is substantiated by the overall more negative nonpolar energy for the CR clusters, than for the other ligands (Figure 12b). It is observed in many of the clusters that CR is positioned diagonally across the top or bottom faces of the fibril and not protruding into the cleft between the isoleucine or phenylalanine side chains, respectively (Figure S6). This enables the sulfate and amino groups of CR to make hydrogen bonds to the serine and asparagine side chains of the fibril. Even if CR is binding to the bottom surface, these polar side chains are observed to relocate to accommodate such hydrogen-bond interaction (CR-C_{lig1}). The shortest distance from any hydrogen-bond donor or acceptor in CR to any donor or acceptor in the serine and asparagine side chains of the fibril is shown in Figure 13. It is clear that at least one hydrogen bond is present throughout most of the simulations for CR-A_{lig2}

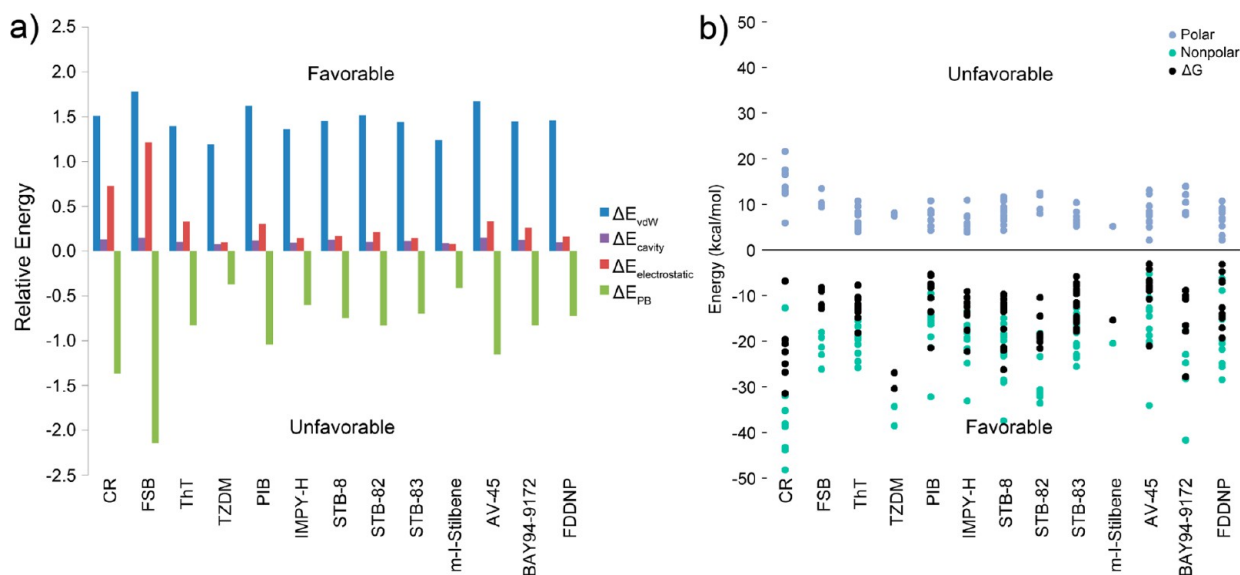


Figure 12. (a) Average relative contribution to the binding energy by the energetic components. Positive values constitute a favorable contribution to the energy. The gas-phase energetic contributions are the van der Waals (E_{vdW}) and electrostatic ($E_{\text{electrostatic}}$) energies. The solvation energy is divided into a polar term (E_{PB}) and a nonpolar term (E_{cavity}). (b) Nonpolar ($E_{\text{vdW}} + E_{\text{cavity}}$, marked as green dots) and polar ($E_{\text{PB}} + E_{\text{electrostatic}}$, marked as purple dots) contributions to the free energy of binding (ΔG , marked with black dots) of all clusters for the 13 ligands.

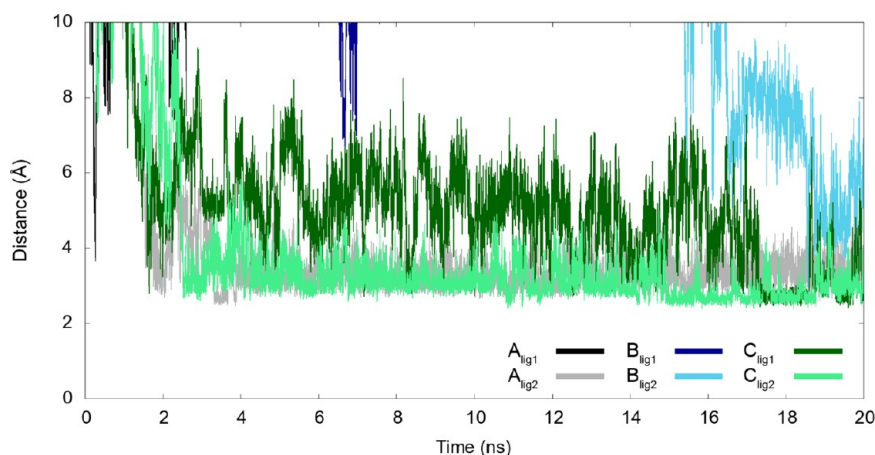


Figure 13. The shortest distance from any hydrogen-bond donor or acceptor heavy atom in CR to any donor or acceptor heavy atom in the serine and asparagine side chains of the fibril.

and CR- C_{lig2} . CR- C_{lig1} is binding on the bottom face, and it is clear that the hydrogen-bond interaction is transiently present, which reflects that the serine and asparagine side chains have to break the β -sheet interaction at the side of the fibril to accommodate the interaction with the hydrophilic groups of CR.

DISCUSSION

We have investigated the binding of 13 different imaging agents and dye molecules to a segment of an amyloid fibril. The ligands in this study are generally elongated, rigid, and aromatic amyloid binding compounds. Some of the ligands share the same scaffold, such as ThT, TZDM, PIB, and IMPY-H, whereas several styryl-based compounds were considered as was indicated in Scheme 1.

Three types of binding sites for imaging agents on amyloid fibrils formed by $A\beta$ have been found, referred to as the CR-, ThT-, and FDDNP-type binding sites.^{56,78,116} The styryl-based compounds have been found to bind in the same binding sites

as the ThT class of compounds.⁵⁶ Classification as belonging to one of the three binding sites depends on which of the three molecules competitively inhibits the binding. Due to the similarity across amyloid fibril structure, similar observations may also apply to amyloid fibrils formed by other peptides. The ligands in this study contain compounds from all three groups (Scheme 1). It was not possible to distinguish the binding sites for the three ligand groups in this study, which may be due to the small size of the fibril model. All ligands seemed to favor the same two binding modes, $\text{top}_{\text{fibril}}^{\text{groove}}$ and $\text{bottom}_{\text{fibril}}^{\text{groove}}$, however with subtle differences based on the particular functionalities of the ligands.

The degree of burial of the ligands seems to play a key role in determining the binding energy for the more nonpolar ligands. Deeper burial was possible in $\text{top}_{\text{fibril}}^{\text{groove}}$ than in $\text{bottom}_{\text{fibril}}^{\text{groove}}$ without the loss of affinity due to strain or steric clashes. Recently, it was also suggested based on MD simulations that the higher binding affinity of PIB over ThT was due to the

ability of PIB to insert deeper into the surface grooves on an amyloid fibril.⁷⁶

Both CR and FSB are elongated molecules with two negative charges, one at each end of the molecule. They share a tendency to bind diagonally on the top and bottom face in the grooves. This may be due to the negative charges that are attracted to the asparagine and serine residues which protrude at the edge of the top surface of the β -sheets. The lower burial percentages of CR and FSB also indicate that the negative charges prevent the molecules from inserting properly in the grooves on the fibril, thereby keeping the charge moiety in the solvent phase. As expected, the electrostatic contribution to the energy was more pronounced for CR and FSB than for the other ligands. It has been shown that the distance between the negative charges on CR is important for the binding to amyloid fibrils.¹¹⁷

Recently, docking calculations of CR to an ss-NMR structure of an amyloid fibril composed of the HET-s peptide were performed.¹¹⁸ These indicated that CR may be oriented along the fibril axis, which is in accordance with the preferred position found in this study, in the top^{groove}_{fibril} and bottom^{groove}_{fibril} binding modes. In this way the negative charges of CR can be counterbalanced by positively charged lysine side chains of the HET-s peptide. Mutation of the lysine residues to alanine removed the positive charge as well as the binding of CR to the fibril, while still retaining the structure of the amyloid fibril.¹¹⁸ The importance of polar/charged interactions for CR was also highlighted in the present MD simulations of binding to the NFGALLS fibrils mimicking hIAPP fibrils by the preference for a binding mode extending diagonally on the top face. This makes interactions possible between the polar asparagine and serine side chains and the negative charges on CR. The contributions to the energy for both CR and FSB are dominated by favorable electrostatic and unfavorable polar desolvation interactions.

The ThT series of compounds display binding to many of the faces of the fibril, except for TZDM. This compound binds to the fibril in only one instance; although, this is a very favorable binding mode in the top, central groove. PIB also shares this binding mode. ThT binds on the top surface as well but does not position itself into the groove. This may be due to the positive charge on ThT which prevents it from inserting deeper into the groove, as has also been observed previously from MD simulations of A β fibrils.⁷⁶ The ThT analog, IMPY-H, displays dimerization in one of the simulations, similar to what has been suggested for excited ThT molecules.^{113,114} ThT is one of the few ligands that shows binding in the top_{normal} binding mode. This is consistent with recent ss-NMR measurements of ThT binding to hIAPP fibrils which showed the presence of two different species, a strongly bound species and a weaker bound species, the latter in the perpendicular orientation.⁶⁹ Two binding modes were proposed: one with ThT parallel to the fibril normal, consistent with top_{normal} (−10 kcal/mol), and one which is consistent with the channel model as well as the presently identified most favorable binding mode for ThT, bottom^{groove}_{fibril} (−24 kcal/mol), where ThT is binding in a hydrophobic surface groove on the fibril.⁶⁹ It has also previously been shown that multiple binding sites of ThT and analogues are present, though no structural information was provided.⁷⁰ MD simulations of ThT and a neutral analog, 2-(4'-methylaminophenyl) benzothiazole (BTA-1), binding to a small fibril formed by fragments of the A β peptide also revealed two types of binding modes for ThT.⁷⁵ One where the

molecules are orientated parallel to the fibril axis, similar to the top^{groove}_{fibril} and bottom^{groove}_{fibril} binding modes, and one where the molecules were positioned at the ends. Our results are comparable to this study of ThT and BTA-1.⁷⁵

FDDNP is the only molecule in its category included in this study. In two of the three simulations, the two FDDNP molecules form a dimer in the solution before binding to the fibril. The formation of a dimer before binding is also seen in one simulation with AV-45 and one with IMPY-H. Similar to the ThT series of compounds, two distinct binding sites on A β fibrils have been observed experimentally for FDDNP.¹¹⁶ In this study we observe FDDNP binding to both the bottom surface and the side of the fibril (Figure S6). This could account for, respectively, the high- and low-affinity binding sites observed for FDDNP.¹¹⁶

The results presented here indicate that a common binding mode for imaging agents is indeed present, however, the exact binding position may vary. A common binding mode in the surface grooves, parallel to the fibril axis, is likely present for amyloid imaging agents. However, the side chains of the fibril as well as the ligand composition will determine the most favorable position of the ligands. So, more polar ligands will seek to bind close to polar amino acids and *vice versa* for nonpolar ligands. This was reflected in the differences in the energetic components making up the binding energy, where polar and charged ligands had larger contributions from the electrostatic and solvation energies than the more nonpolar ligands. The structure as well as the sequence of an amyloid fibril determines the characteristics of the grooves on the surface. Therefore, even though amyloid imaging agents could all bind in surface grooves, subtle differences of the ligands as well as the morphology of the fibril may determine the particular binding position and affinity of a ligand for an amyloid fibril. Further studies are in progress to experimentally test the hypothesis of a common binding mode and to expand the concept to include other amyloid fibrils, including amyloid- β .

■ ASSOCIATED CONTENT

⑤ Supporting Information

Simulation data for the ligands not included in the main manuscript, a table containing the energy decomposition for the clusters, and the ligand force field parameters. This material is available free of charge via the Internet at <http://pubs.acs.org>.

■ AUTHOR INFORMATION

Corresponding Author

birgit@chem.au.dk

Present Address

[†]Department of Chemistry and Biochemistry, University of California, San Diego, La Jolla, CA 92093.

Notes

The authors declare no competing financial interest.

■ ACKNOWLEDGMENTS

Troels Skrydstrup and Niels Chr. Nielsen, iNANO, Aarhus University, are thanked for fruitful suggestions and discussions. This work was supported by grants from the Danish Council for Independent Research | Technology and Production Sciences (FTP), the Danish National Research Foundation (DNRF59), and the Centre for Theory in Natural Sciences, Aarhus University. Computations were made possible through

grants from the Danish Center for Scientific Computing. J.S. is grateful for funding from the Alfred Benzon Foundation through a postdoctoral fellowship. Cover Background Photo Copyright openclipart.org.

REFERENCES

- (1) Harrison, R. S.; Sharpe, P. C.; Singh, Y.; Fairlie, D. P. *Rev. Physiol. Biochem. Pharmacol.* **2007**, 159, 1–77.
- (2) Chiti, F.; Dobson, C. M. *Annu. Rev. Biochem.* **2006**, 75, 333–366.
- (3) O’Nuallain, B.; Williams, A. D.; Westermarck, P.; Wetzel, R. J. *Biol. Chem.* **2004**, 279, 17490–17499.
- (4) Geddes, A. J.; Parker, K. D.; Atkins, E. D. T.; Beighton, E. J. *Mol. Biol.* **1968**, 32, 343–358.
- (5) Sunde, M.; Serpell, L.; Bartlam, M.; Fraser, P. E.; Pepys, M. B.; Blake, C. C. F. *J. Mol. Biol.* **1997**, 273, 729–739.
- (6) Greenwald, J.; Riek, R. *Structure* **2010**, 18, 1244–1260.
- (7) Fändrich, M. *Cell. Mol. Life Sci.* **2007**, 64, 2066–2078.
- (8) Qiang, W.; Yau, W.; Luo, Y.; Mattson, M. P.; Tycko, R. *Proc. Natl. Acad. Sci. U.S.A.* **2012**, 109, 4443–4448.
- (9) Shewmaker, F.; McGlinchey, R. P.; Wickner, R. B. *J. Biol. Chem.* **2011**, 286, 16533–16540.
- (10) Petkova, A. T.; Ishii, Y.; Balbach, J. J.; Antzutkin, O. N.; Leapman, R. D.; Delaglio, F.; Tycko, R. *Proc. Natl. Acad. Sci. U.S.A.* **2002**, 99, 16742–16747.
- (11) Paravastu, A. K.; Leapman, R. D.; Yau, W.; Tycko, R. *Proc. Natl. Acad. Sci. U.S.A.* **2008**, 105, 18349–18354.
- (12) Bertini, I.; Gonnelli, L.; Luchinat, C.; Mao, J.; Nesi, A. *J. Am. Chem. Soc.* **2011**, 133, 16013–16022.
- (13) Bedrood, S.; Li, Y.; Isas, J. M.; Hegde, B. G.; Baxa, U.; Haworth, I. S.; Langen, R. *J. Biol. Chem.* **2012**, 287, 5235–5241.
- (14) McDonald, M.; Box, H.; Bian, W.; Kendall, A.; Tycko, R.; Stubbs, G. *J. Mol. Biol.* **2012**, 423, 454–461.
- (15) Toyama, B. H.; Weissman, J. S. *Annu. Rev. Biochem.* **2011**, 80, 557–585.
- (16) Tycko, R. *Annu. Rev. Phys. Chem.* **2011**, 62, 279–299.
- (17) Nelson, R.; Sawaya, M. R.; Balbirnie, M.; Madsen, A. Ø.; Riek, C.; Grothe, R.; Eisenberg, D. *Nature* **2005**, 435, 773–778.
- (18) Sawaya, M. R.; Sambashivan, S.; Nelson, R.; Ivanova, M. B.; Sievers, S. A.; Apostol, M. I.; Thompson, M. J.; Balbirnie, M.; Wiltzius, J. J. W.; McFarlane, H. T.; Madsen, A. Ø.; Riek, C.; Eisenberg, D. *Nature* **2007**, 447, 453–457.
- (19) Apostol, M. I.; Sawaya, M. R.; Cascio, D.; Eisenberg, D. *J. Biol. Chem.* **2010**, 285, 29671–29675.
- (20) Periole, X.; Rampioni, A.; Vendruscolo, M.; Mark, A. E. *J. Phys. Chem. B* **2009**, 113, 1728–1737.
- (21) Westermarck, P.; Engstrom, U.; Johnson, K. H.; Westermarck, G. T.; Betsholtz, C. *Proc. Natl. Acad. Sci. U.S.A.* **1990**, 87, 5036–5040.
- (22) Tenidis, K.; Waldner, M.; Bernhagen, J.; Fischle, W.; Bergmann, M.; Weber, M.; Merkle, M. L.; Voelter, W.; Brunner, H.; Kapurniotu, A. *J. Mol. Biol.* **2000**, 295, 1055–1071.
- (23) Zhang, S.; Andreasen, M.; Nielsen, J. T.; Liu, L.; Nielsen, E. H.; Song, J.; Ji, G.; Sun, F.; Skrydstrup, T.; Besenbacher, F.; Nielsen, N. C.; Otzen, D. E.; Dong, M. *Proc. Natl. Acad. Sci. U.S.A.* **2013**, 110, 2798–2803.
- (24) Murphy, R. M. *Biochim. Biophys. Acta, Biomembr.* **2007**, 1768, 1923–1934.
- (25) Pellarin, R.; Caffisch, A. *J. Mol. Biol.* **2006**, 360, 882–892.
- (26) Pellarin, R.; Guarniera, E.; Caffisch, A. *J. Mol. Biol.* **2007**, 374, 917–924.
- (27) Friedman, R.; Pellarin, R.; Caffisch, A. *J. Mol. Biol.* **2009**, 387, 407–415.
- (28) Sørensen, J.; Periole, X.; Skeby, K. K.; Marrink, S.-J.; Schiøtt, B. *J. Phys. Chem. B* **2011**, 2, 2385–2390.
- (29) Sørensen, J.; Hamelberg, D.; Schiøtt, B.; McCammon, J. A. *Biopolymers* **2007**, 86, 73–82.
- (30) Friedman, R. *Biochem. J.* **2011**, 438, 415–426.
- (31) Zanuy, D.; Gunasekaran, K.; Ma, B. Y.; Tsai, H. H.; Tsai, C. J.; Nussinov, R. *Amyloid* **2004**, 11, 143–161.
- (32) Engel, M. F. M.; Khemtemourian, L.; Kleijer, C. C.; Meeldijk, H. J. D.; Jacobs, J.; Verkleij, A. J.; de Kruijff, B.; Killian, J. A.; Hoepfner, J. W. M. *Proc. Natl. Acad. Sci. U.S.A.* **2008**, 105, 6033–6038.
- (33) Stefani, M. *FEBS J.* **2010**, 277, 4602–4613.
- (34) Cao, P.; Marek, P.; Noor, H.; Patsalo, V.; Tu, L.; Wang, H.; Abedini, A.; Raleigh, D. P. *FEBS Lett.* **2013**, 587, 1106–1118.
- (35) Abedini, A.; Schmidt, A. M. *FEBS Lett.* **2013**, 587, 1119–1127.
- (36) Nordberg, A. *Lancet Neurol.* **2004**, 3, 519–527.
- (37) Nordberg, A. *Neurodegener. Dis.* **2010**, 7, 136–138.
- (38) Furumoto, S.; Okamura, N.; Iwata, R.; Yanai, K.; Arai, H.; Kudo, Y. *Curr. Top. Med. Chem.* **2007**, 7, 1773–1789.
- (39) Klunk, W. E.; Engler, H.; Nordberg, A.; Wang, Y. M.; Blomqvist, G.; Holt, D. P.; Bergstrom, M.; Savitcheva, I.; Huang, G. F.; Estrada, S.; Aussen, B.; Debnath, M. L.; Barletta, J.; Price, J. C.; Sandell, J.; Lopresti, B. J.; Wall, A.; Koivisto, P.; Antoni, G.; Mathis, C. A.; Langstrom, B. *Ann. Neurol.* **2004**, 55, 306–319.
- (40) Shoghi-Jadid, K.; Small, G. W.; Agdeppa, E. D.; Kepe, V.; Ercoli, L. M.; Siddarth, P.; Read, S.; Satyamurthy, N.; Petric, A.; Huang, S. C.; Barrio, J. R. *Am. J. Geriatr. Psychiatry* **2002**, 10, 24–35.
- (41) Newberg, A. B.; Wintering, N. A.; Plossl, K.; Hochold, J.; Stabin, M. G.; Watson, M.; Skovronsky, D.; Clark, C. M.; Kung, M. P.; Kung, H. F. *J. Nucl. Med.* **2006**, 47, 748–754.
- (42) McKhann, G.; Drachman, D.; Folstein, M.; Katzman, R.; Price, D.; Stadlan, E. M. *Neurology* **1984**, 34, 939–944.
- (43) Zamrini, E.; De Santi, S.; Tolar, M. *Neurobiol. Aging* **2004**, 25, 685–691.
- (44) Dickerson, B. C.; Sperling, R. A. *NeuroRx* **2005**, 2, 348–360.
- (45) Thal, L. J.; Kantarci, K.; Reiman, E. M.; Klunk, W. E.; Weiner, M. W.; Zetterberg, H.; Galasko, D.; Pratico, D.; Griffin, S.; Schenk, D.; Siemers, E. *Alzheimer Dis. Assoc. Disord.* **2006**, 20, 6–15.
- (46) Mathis, C. A.; Lopresti, B. J.; Klunk, W. E. *Nucl. Med. Biol.* **2007**, 34, 809–822.
- (47) Howie, A. J.; Brewer, D. B. *Micron* **2009**, 40, 285–301.
- (48) Porat, Y.; Abramowitz, A.; Gazit, E. *Chem. Biol. Drug Des.* **2006**, 67, 27–37.
- (49) Caughey, B.; Ernst, D.; Race, R. E. *J. Virol.* **1993**, 67, 6270–6272.
- (50) Kim, Y. S.; Randolph, T. W.; Manning, M. C.; Stevens, F. J.; Carpenter, J. F. *J. Biol. Chem.* **2003**, 278, 10842–10850.
- (51) Lorenzo, A.; Yankner, B. A. *Proc. Natl. Acad. Sci. U.S.A.* **1994**, 91, 12243–12247.
- (52) Biancalana, M.; Koide, S. *Biochim. Biophys. Acta, Proteins Proteomics* **2010**, 1804, 1405–1412.
- (53) Fodera, V.; Librizzi, F.; Groenning, M.; van de Weert, M.; Leone, M. *J. Phys. Chem. B* **2008**, 112, 3853–3858.
- (54) Nielsen, L.; Khurana, R.; Coats, A.; Frokjaer, S.; Brange, J.; Vyas, S.; Uversky, V. N.; Fink, A. L. *Biochemistry* **2001**, 40, 6036–6046.
- (55) Mauro, M.; Craparo, E. F.; Podesta, A.; Bulone, D.; Carrota, R.; Martorana, V.; Tiana, G.; San Biagio, P. L. *J. Mol. Biol.* **2007**, 366, 258–274.
- (56) Cai, L.; Innis, R. B.; Pike, V. W. *Curr. Med. Chem.* **2007**, 14, 19–52.
- (57) Mathis, C. A.; Wang, Y. M.; Holt, D. P.; Huang, G. F.; Debnath, M. L.; Klunk, W. E. *J. Med. Chem.* **2003**, 46, 2740–2754.
- (58) Small, G. W.; Kepe, V.; Ercoli, L. M.; Siddarth, P.; Bookheimer, S. Y.; Miller, K. J.; Lavretsky, H.; Burggren, A. C.; Cole, G. M.; Vinters, H. V.; Thompson, P. M.; Huang, S.-C.; Satyamurthy, N.; Phelps, M. E.; Barrio, J. R. *N. Engl. J. Med.* **2006**, 355, 2652–2663.
- (59) Choi, S. R.; Golding, G.; Zhuang, Z.; Zhang, W.; Lim, N.; Hefti, F.; Benedum, T. E.; Kilbourn, M. R.; Skovronsky, D.; Kung, H. F. *J. Nucl. Med. (USA)* **2009**, 50, 1887–1894.
- (60) Grill, J. D.; Johnson, D. K.; Burns, J. M. *Neurodegen. Dis. Manage.* **2013**, 3, 43–51.
- (61) Li, Q.; Min, J.; Ahn, Y.; Namm, J.; Kim, E. M.; Lui, R.; Kim, H. Y.; Ji, Y.; Wu, H.; Wisniewski, T.; Chang, Y. *ChemBioChem* **2007**, 8, 1679–1687.
- (62) Verhoeff, N. P. L. G.; Wilson, A. A.; Takeshita, S.; Trop, L.; Hussey, D.; Singh, K.; Kung, H. F.; Kung, M. P.; Houle, S. *Am. J. Geriatr. Psychiatry* **2004**, 12, 584–595.

- (63) Rowe, C. C.; Ackerman, U.; Browne, W.; Mulligan, R.; Pike, K. L.; O'Keefe, G.; Tochon-Danguy, H.; Chan, G.; Berlangieri, S. U.; Jones, G.; Dickinson-Rowe, K. L.; Kung, H. P.; Zhang, W.; Kung, M. P.; Skovronsky, D.; Dyrks, T.; Hall, G.; Krause, S.; Friebe, M.; Lehman, L.; Lindemann, S.; Dinkelborg, L. M.; Masters, C. L.; Villemagne, V. L. *Lancet Neurol.* **2008**, *7*, 129–135.
- (64) Kudo, Y.; Okamura, N.; Furumoto, S.; Tashiro, M.; Furukawa, K.; Maruyama, M.; Itoh, M.; Iwata, R.; Yanai, K.; Arai, H. *J. Nucl. Med.* **2007**, *48*, 553–561.
- (65) Koole, M.; Lewis, D. M.; Buckley, C.; Nelissen, N.; Vandenbulcke, M.; Brooks, D. J.; Vandenbergh, R.; Van Laere, K. J. *Nucl. Med.* **2009**, *50*, 818–822.
- (66) Wong, D. F.; Rosenberg, P. B.; Zhou, Y.; Kumar, A.; Raymont, V.; Ravert, H. T.; Dannals, R. F.; Nandi, A.; Brasic, J. R.; Ye, W.; Hilton, J.; Lyketsos, C.; Kung, H. F.; Joshi, A. D.; Skovronsky, D. M.; Pontecorvo, M. J. *J. Nucl. Med.* **2010**, *51*, 913–920.
- (67) Nordberg, A.; Rinne, J. O.; Kadir, A.; Langstrom, B. *Nat. Rev. Neurol.* **2010**, *6*, 78–87.
- (68) Krebs, M. R. H.; Bromley, E. H. C.; Donald, A. M. *J. Struct. Biol.* **2005**, *149*, 30–37.
- (69) Robbins, K. J.; Liu, G.; Lin, G.; Lazo, N. D. *J. Phys. Chem. Lett.* **2011**, *2*, 735–740.
- (70) Lockhart, A.; Ye, L.; Judd, D. B.; Merritt, A. T.; Lowe, P. N.; Morgenstern, J. L.; Hong, G. Z.; Gee, A. D.; Brown, J. J. *Biol. Chem.* **2005**, *280*, 7677–7684.
- (71) Wu, C.; Lei, H.; Wang, Z.; Zhang, W.; Duan, Y. *Biophys. J.* **2006**, *91*, 3664–3672.
- (72) Lemkul, J. A.; Bevan, D. R. *Biochemistry* **2010**, *49*, 3935–3946.
- (73) Berhanu, W. M.; Masunov, A. E. *Biophys. Chem.* **2010**, *149*, 12–21.
- (74) Wu, C.; Wang, Z.; Lei, H.; Zhang, W.; Duan, Y. *J. Am. Chem. Soc.* **2007**, *129*, 1225–1232.
- (75) Wu, C.; Wang, Z.; Lei, H.; Duan, Y.; Bowers, M. T.; Shea, J. J. *Mol. Biol.* **2008**, *384*, 718–729.
- (76) Wu, C.; Bowers, M. T.; Shea, J. *Biophys. J.* **2011**, *100*, 1316–1324.
- (77) Lemkul, J. A.; Bevan, D. R. *ACS Chem. Neurosci.* **2012**, *3*, 845–856.
- (78) Zhuang, Z. P.; Kung, M. P.; Hou, C.; Skovronsky, D. M.; Gur, T. L.; Plossl, K.; Trojanowski, J. Q.; Lee, V. M. Y.; Kung, H. F. *J. Med. Chem.* **2001**, *44*, 1905–1914.
- (79) Kung, M.; Hou, C.; Zhuang, Z.; Skovronsky, D.; Kung, H. *Brain Res.* **2004**, *1025*, 98–105.
- (80) Nielsen, J. T.; Bjerring, M.; Jeppesen, M. D.; Pedersen, R. O.; Pedersen, J. M.; Hein, K. L.; Vosegaard, T.; Skrydstrup, T.; Otzen, D.; Nielsen, N. C. *Angew. Chem., Int. Ed.* **2009**, *48*, 2118–2121.
- (81) Cooper, G. J. S.; Willis, A. C.; Clark, A.; Turner, R. C.; Sim, R. B.; Reid, K. B. M. *Proc. Natl. Acad. Sci. U.S.A.* **1987**, *84*, 8628–8632.
- (82) Westermarck, P.; Wernstedt, C.; Wilander, E.; Hayden, D. W.; O'Brien, T. D.; Johnson, K. H. *Proc. Natl. Acad. Sci. U.S.A.* **1987**, *84*, 3881–3885.
- (83) Duan, Y.; Wu, C.; Chowdhury, S.; Lee, M. C.; Xiong, G.; Zhang, W.; Yang, R.; Cieplak, P.; Luo, R.; Lee, T.; Caldwell, J.; Wang, J.; Kollman, P. A. *J. Comput. Chem.* **2003**, *24*, 1999–2012.
- (84) Schrödinger LLC **2008** Schrödinger Suite 2008, Maestro Version 8.5, MacroModel Version 9.6.
- (85) Polak, E.; Ribiere, G. *Rev. Fr. Inform. Rech. Oper.* **1969**, *3*, 35–43.
- (86) Kolossváry, I.; Guida, W. C. *J. Am. Chem. Soc.* **1996**, *118*, 5011–5019.
- (87) Kolossváry, I.; Guida, W. C. *J. Comput. Chem.* **1999**, *20*, 1671–1684.
- (88) Jorgensen, W. L.; Maxwell, D. S.; Tirado-Rives, J. *J. Am. Chem. Soc.* **1996**, *118*, 11225–11236.
- (89) Still, W. C.; Tempczyk, A.; Hawley, R. C.; Hendrickson, T. J. *Am. Chem. Soc.* **1990**, *112*, 6127–6129.
- (90) Frisch, M. J.; Trucks, G. W.; Schlegel, H. B.; Scuseria, G. E.; Robb, M. A.; Cheeseman, J. R.; Montgomery, J. A., Jr.; Vreven, T.; Kudin, K. N.; Burant, J. C.; Millam, J. M.; Iyengar, S. S.; Tomasi, J.; Barone, V.; Mennucci, B.; Cossi, M.; Scalmani, G.; Rega, N.; Petersson, G. A.; Nakatsuji, H.; Hada, M.; Ehara, M.; Toyota, K.; Fukuda, R.; Hasegawa, J.; Ishida, M.; Nakajima, T.; Honda, Y.; Kitao, O.; Nakai, H.; Klene, M.; Li, X.; Knox, J. E.; Hratchian, H. P.; Cross, J. B.; Bakken, V.; Adamo, C.; Jaramillo, J.; Gomperts, R.; Stratmann, R. E.; Yazyev, O.; Austin, A. J.; Cammi, R.; Pomelli, C.; Ochterski, J. W.; Ayala, P. Y.; Morokuma, K.; Voth, G. A.; Salvador, P.; Dannenberg, J. J.; Zakrzewski, V. G.; Dapprich, S.; Daniels, A. D.; Strain, M. C.; Farkas, O.; Malick, D. K.; Rabuck, A. D.; Raghavachari, K.; Foresman, J. B.; Ortiz, J. V.; Cui, Q.; Baboul, A. G.; Clifford, S.; Cioslowski, J.; Stefanov, B. B.; Liu, G.; Liashenko, A.; Piskorz, P.; Komaromi, I.; Martin, R. L.; Fox, D. J.; Keith, T.; Al-Laham, M. A.; Peng, C. Y.; Nanayakkara, A.; Challacombe, M.; Gill, P. M. W.; Johnson, B.; Chen, W.; Wong, M. W.; Gonzalez, C.; Pople, J. A. *Gaussian 03*; Gaussian, Inc.: Wallingford, CT, 2004.
- (91) Wang, J.; Wolf, R. M.; Caldwell, J. W.; Kollman, P. A.; Case, D. A. *J. Comput. Chem.* **2004**, *25*, 1157–1174.
- (92) Case, D. A.; Darden, T. A.; Cheatham, T. E. I.; Simmerling, C.; Wang, J.; Duke, R. E.; Luo, R.; Merz, K. M.; Pearlman, D. A.; Crowley, M.; Walker, R. C.; Zhang, W.; Wang, B.; Hayik, S.; Roitberg, A.; Seabra, G.; Wong, K. F.; Paesani, F.; Wu, X.; Brozell, S.; Tsui, V.; Gohlke, H.; Yang, L.; Tan, C.; Mongan, J.; Hornak, V.; Cui, C.; Beroza, P.; Mathews, D. H.; Shafmeister, C.; Ross, W. S.; Kollman, P. A. *AMBER 9*; University of California, San Francisco: San Francisco, CA, 2006.
- (93) Bayly, C.; Cieplak, P.; Cornell, W. D.; Kollman, P. A. *J. Phys. Chem.* **1993**, *97*, 10269–10280.
- (94) Jorgensen, W. L.; Chandrasekhar, J.; Madura, J. D.; Impey, R. W.; Klein, M. L. *J. Chem. Phys.* **1983**, *79*, 926–935.
- (95) Phillips, J. C.; Braun, R.; Wang, W.; Gumbart, J.; Tajkhorshid, E.; Villa, E.; Chipot, C.; Skeel, R. D.; Kalé, L.; Schulten, K. *J. Comput. Chem.* **2005**, *26*, 1781–1802.
- (96) Ryckaert, J. P.; Ciccotti, G.; Berendsen, H. J. C. *J. Comput. Phys.* **1977**, *23*, 327–341.
- (97) Weinbach, Y.; Elber, R. *J. Comput. Phys.* **2005**, *209*, 193–206.
- (98) Nose, S.; Klein, M. L. *Mol. Phys.* **1983**, *50*, 1055–1076.
- (99) Hoover, W. G. *Phys. Rev. A* **1985**, *31*, 1695–1697.
- (100) Martyna, G. J.; Tobias, D. J.; Klein, M. L. *J. Chem. Phys.* **1994**, *101*, 4177–4189.
- (101) Ewald, P. P. *Ann. Phys.* **1921**, *64*, 253–287.
- (102) Darden, T.; York, D.; Pedersen, L. J. *Chem. Phys.* **1993**, *98*, 10089–10092.
- (103) York, D. M.; Wlodawer, A.; Pedersen, L. G.; Darden, T. A. *Proc. Natl. Acad. Sci. U.S.A.* **1994**, *91*, 8715–8718.
- (104) Jain, A.; Murty, M.; Flynn, P. *ACM Comput. Surv.* **1999**, *31*, 264–323.
- (105) Case, D. A.; Darden, T. A.; Cheatham, T. E., III; Simmerling, C. L.; Wang, J.; Duke, R. E.; Luo, R.; Walker, R. C.; Zhang, W.; Merz, K. M.; Roberts, B.; Wang, B.; Hayik, S.; Roitberg, A.; Seabra, G.; Kolossváry, I.; Wong, K. F.; Paesani, F.; Vanicek, J.; Liu, J.; Wu, X.; Brozell, S. R.; Steinbrecher, T.; Gohlke, H.; Cai, Q.; Ye, X.; Wang, J.; Hsieh, M.-J.; Cui, G.; Roe, D. R.; Mathews, D. H.; Seetin, M. G.; Sagui, C.; Babin, V.; Luchko, T.; Gusarov, S.; Kovalenko, A.; Kollman, P. A. *AMBER 11*; University of California, San Francisco: San Francisco, CA, 2010.
- (106) Srinivasan, J.; Cheatham, T. E. I.; Cieplak, P.; Kollman, P. A.; Case, D. A. *J. Am. Chem. Soc.* **1998**, *120*, 9401–9409.
- (107) Kollman, P. A.; Massova, I.; Reyes, C.; Kuhn, B.; Huo, S.; Chong, L.; Lee, M.; Lee, T.; Duan, Y.; Wang, W.; Donini, O.; Cieplak, P.; Srinivasan, J.; Case, D. A.; Cheatham, T. E. I. *Acc. Chem. Res.* **2000**, *33*, 889–897.
- (108) Hou, T.; Wang, J.; Li, Y.; Wang, W. *J. Chem. Inf. Model.* **2011**, *51*, 69–82.
- (109) Donini, O.; Kollman, P. *J. Med. Chem.* **2000**, *43*, 4180–4188.
- (110) Swanson, J. M. J.; Henchman, R. H.; McCammon, J. A. *Biophys. J.* **2004**, *86*, 67–74.
- (111) Miller, B. R.; McGee, T. D.; Swails, J. M.; Homeyer, N.; Gohlke, H.; Roitberg, A. E. *J. Chem. Theory Comput.* **2012**, *8*, 3314–3321.
- (112) Zanuy, D.; Nussinov, R. *J. Mol. Biol.* **2003**, *329*, 565–584.

- (113) Groenning, M.; Olsen, L.; van de Weert, M.; Flink, J. M.; Frokjaer, S.; Jorgensen, F. S. *J. Struct. Biol.* **2007**, *158*, 358–369.
- (114) Groenning, M.; Norrman, M.; Flink, J. M.; van de Weert, M.; Bukrinsky, J. T.; Schluckebier, G.; Frokjaer, S. *J. Struct. Biol.* **2007**, *159*, 483–497.
- (115) Hård, T.; Lendel, C. *J. Mol. Biol.* **2012**, *421*, 441–465.
- (116) Agdeppa, E. D.; Kepe, V.; Liu, J.; Flores-Torres, S.; Satyamurthy, N.; Petric, A.; Cole, G. M.; Small, G. W.; Huang, S. C.; Barrio, J. R. *J. Neurosci.* **2001**, *21*, RC189.
- (117) Ashburn, T. T.; Han, H.; McGuinness, B. F.; Lansbury, P. T., Jr. *Chem. Biol.* **1996**, *3*, 351–358.
- (118) Schütz, A. K.; Soragni, A.; Hornemann, S.; Aguzzi, A.; Ernst, M.; Boeckmann, A.; Meier, B. H. *Angew. Chem., Int. Ed.* **2011**, *50*, 5956–5960.